

KIT SCIENTIFIC REPORTS 7713

# **Numerical simulations of MHD flow transition in ducts with conducting Hartmann walls**

Limtech Project A3 D4 (TUI)

D. Krasnov, T. Boeck, L. Braiden, S. Molokov, L. Bühler



D. Krasnov, T. Boeck, L. Braiden, S. Molokov, L. Bühler

**Numerical simulations of MHD flow transition  
in ducts with conducting Hartmann walls**

Limtech Project A3 D4 (TUI)

**Karlsruhe Institute of Technology**  
**KIT SCIENTIFIC REPORTS 7713**

# Numerical simulations of MHD flow transition in ducts with conducting Hartmann walls

Limtech Project A3 D4 (TUI)

von

**D. Krasnov, T. Boeck**

Institute of Thermodynamics and Fluid Mechanics | Technische Universität Ilmenau (TUI)

**L. Braiden, S. Molokov**

Department of Mathematics and Physics | Coventry University (CU)

**L. Bühler**

Institut für Kern- und Energietechnik (IKET-KIT) | Programm Kernfusion (KIT)

## Report-Nr. KIT-SR 7713

### Impressum



Karlsruher Institut für Technologie (KIT)  
KIT Scientific Publishing  
Straße am Forum 2  
D-76131 Karlsruhe

KIT Scientific Publishing is a registered trademark of Karlsruhe  
Institute of Technology. Reprint using the book cover is not allowed.

[www.ksp.kit.edu](http://www.ksp.kit.edu)



*This document – excluding the cover, pictures and graphs – is licensed  
under the Creative Commons Attribution-Share Alike 3.0 DE License  
(CC BY-SA 3.0 DE): <http://creativecommons.org/licenses/by-sa/3.0/de/>*



*The cover page is licensed under the Creative Commons  
Attribution-No Derivatives 3.0 DE License (CC BY-ND 3.0 DE):  
<http://creativecommons.org/licenses/by-nd/3.0/de/>*

Print on Demand 2016

ISSN 1869-9669

ISBN 978-3-7315-0562-4

DOI: 10.5445/KSP/1000057744





## **Acknowledgement**

Financial support of this research by the German Helmholtz Association in the frame of the Helmholtz-Alliance LIMTECH is gratefully acknowledged. Lee Braiden's work is supported by the Culham Centre for Fusion Energy (CCFE), UK. Computer resources were provided by the computing centers of Forschungszentrum Jülich (NIC), TU Ilmenau and Coventry University.



## Abstract

Pressure-driven magnetohydrodynamic duct flows in a transverse, wall-parallel and uniform field have been studied by direct numerical simulations with a conservative finite-difference method based on the quasi-static approximation of the induction equation. The conducting Hartmann walls perpendicular to the magnetic field give rise to a laminar velocity distribution with strong jets at the side walls, which are susceptible to flow instability. A parallel code for perfectly conducting or insulating walls and with streamwise periodicity has been extended to the case of finite wall conductance in the thin-wall approximation. Because of the substantial increase in computational cost associated with the finite wall conductance, high-resolution simulations have mainly been performed with perfectly conducting Hartmann walls and insulating side walls. The onset of time-dependent flow as well as fully-developed turbulent flow have been explored for Hartmann numbers  $Ha$  up to 1000 and Reynolds numbers  $Re$  up to 50000. For the relatively low Hartmann number  $Ha = 100$ , time-dependence appears in the form of elongated so-called Ting-Walker vortices at the side walls of the duct, which tend to form staggered patterns along the streamwise direction. Upon increasing the Reynolds number these vortices are replaced by more complex eddy structures, and the jets partially detach from the walls. Eventually, the flow becomes fully turbulent in the side-wall region. For  $Ha = 1000$  and  $Re = 10000$  the flow displays localized patterns of jet detachments near the side walls, but with more disorder than at  $Ha = 100$ . For higher Reynolds number  $Re = 50000$  the patches are replaced by continuous turbulent bands that occupy the full length of the duct while the core of the flow still remains almost laminar.



## Zusammenfassung

Magnetohydrodynamische Kanalströmungen in einem transversalen, wandparallelen und homogenen Magnetfeld wurden mittels direkter numerische Simulation mit einem konservativen finite-Differenzen-Verfahren auf Grundlage der quasistatischen Näherung der Induktionsgleichung untersucht. Die leitfähigen Hartmannwände senkrecht zum Magnetfeld verursachen eine laminare Geschwindigkeitsverteilung, die durch starke Jets an den Seitenwänden gekennzeichnet ist, weshalb die Strömung zur Instabilität neigt. Ein numerischer Code für ideal leitfähige oder isolierende Wände und mit periodischen Randbedingungen entlang der Strömungsrichtung wurde auf endliche Wandleitfähigkeit erweitert, die im Rahmen der sogenannten "thin-wall" Näherung berücksichtigt wird. Das Einsetzen zeitabhängiger Strömung sowie voll entwickelte Turbulenz wurden für Hartmannzahlen  $Ha$  bis 1000 und Reynoldszahlen  $Re$  bis 50000 untersucht. Für die relativ geringe Hartmannzahl  $Ha = 100$  tritt Zeitabhängigkeit in Form von gestreckten sogenannten Ting-Walker-Wirbeln an den Seitenwänden auf. Diese organisieren sich bevorzugt in versetzten Mustern entlang der Strömungsrichtung. Bei Erhöhung der Reynoldszahl werden diese Wirbel durch komplexere Wirbelstrukturen ersetzt und die Jets lösen sich teilweise von der Wand ab (jet detachment). Schließlich wird die Strömung an den Seitenwänden voll turbulent. Für  $Ha = 1000$  und  $Re = 10000$  zeigt die Strömung lokale Ablösungen in der Nähe der Seitenwand (jet detachment), wobei diese jedoch weniger geordnet sind als bei  $Ha = 100$ . Für die höhere Reynoldszahl  $Re = 10000$  werden diese lokalisierten Bereiche durch turbulente Bänder ersetzt, die die volle Länge des Kanals ausfüllen, wobei die Kernströmung immer nahezu laminar erscheint.



# Contents

<b>1</b>	<b>Introduction</b>	<b>1</b>
<b>2</b>	<b>Mathematical model and numerical method</b>	<b>3</b>
2.1	Governing equations for low- $Re_m$ MHD flows . . . . .	3
2.2	Finite-difference solver . . . . .	4
2.3	Implicit scheme for viscous terms . . . . .	5
2.4	Boundary conditions for finite-wall conductivity . . . . .	6
<b>3</b>	<b>Results of simulations</b>	<b>9</b>
3.1	Benchmarks for laminar duct flow . . . . .	9
3.2	Results at low- $Ha$ regimes, jet detachment . . . . .	10
3.3	Results at high $Ha$ numbers . . . . .	14
3.4	Multiple states at low- $Re$ regimes . . . . .	16
<b>4</b>	<b>Conclusions and outlook</b>	<b>21</b>



# 1 Introduction

Motion of an electrically conducting fluid through an imposed magnetic field generates a Lorentz force, which tends to suppress fluid motion. The mechanism of suppression is either the “braking” effect of the mean velocity or damping of turbulent fluctuations or both. When the applied magnetic field in a wall-bounded flow is perpendicular to the flow direction, the basic velocity is strongly modified, such that a flat core and thin boundary layers develop. Well-known examples are the flows in electrically insulating and conducting ducts as investigated initially by Shercliff and Hunt.

In this study we investigate flow in a square duct with conducting Hartmann walls, i.e. Hunt’s type of flow. From the view of practical applications, conducting metal walls are typically present in cooling devices. One of the most prominent examples here are liquid-metal cooled blankets in future nuclear fusion devices. The blankets contain liquid PbLi alloy for tritium production from Li by neutron radiation. They surround the plasma chamber on the outside and are exposed to the strong magnetic field of the plasma confinement. The PbLi has to be pumped in order to extract tritium and heat.

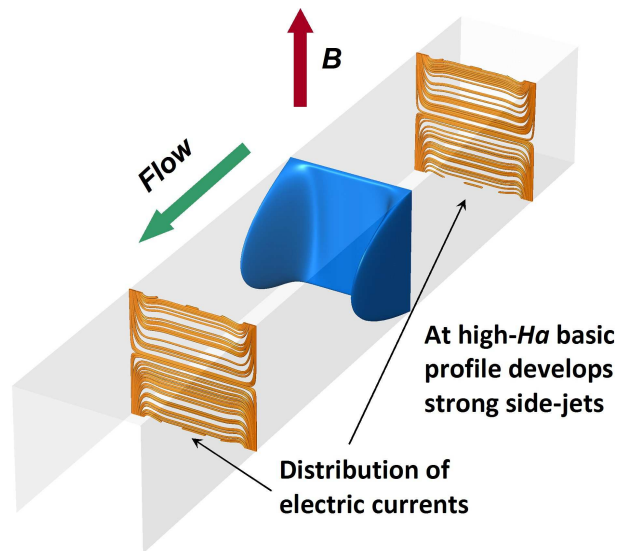


Figure 1: Velocity distribution of laminar Hunt’s flow at a Hartmann number  $Ha = 100$  (blue); also shown are the streamlines of electric current density (brown).

In this geometry, where conducting Hartmann walls are perpendicular to the applied magnetic field, the distribution of induced currents is organized in such a way that the velocity field develops sidewall jets (shown in Fig. 1). A particular feature of this flow is the presence of high shear and the appearance of inflection points the jet-like velocity profile, which can give rise to inviscid Kelvin-Helmholtz instability. In contrast to non-MHD shear flows or Hartmann flow, flow instability may therefore occur at low Reynolds numbers if the magnetic field is sufficiently strong. The prediction and understanding of flow instabilities should be viewed as an important applied problem for designing cooling blankets. For example, it is

important to know the nature of the flow in a cooling blanket, since development of instability and, ultimately, turbulence can significantly intensify flow mixing and enhance heat and mass transfer.

The instability of Hunt's flow has been addressed in prior studies. Small-scale instabilities within the sidewall jets were first predicted by linear stability analysis in Ting *et al.* (1991). The discovered small-scale instabilities are now commonly referred to as Ting-Walker vortices (TW). An example of such instability in the region of sidewall jets is shown in Fig. 2 for the Reynolds number  $Re = 500$ . The linear stability analysis has been extended recently by Priede *et al.* (2010), who identified several solution branches corresponding to unstable regimes. The instability of the side jets has also been observed experimentally in recent studies (Bühler, L. and Horanyi, S., 2009). On the numerical side, however, there are only few simulations to date as, e.g., Kinet *et al.* (2009). In the present work we extend the simulations for a square duct to a broader range of Reynolds numbers and Hartmann numbers  $Ha$ , specifically to high- $Ha$  regimes, which are of particular interest for fusion applications. Another important aspect is that, in parallel to the numerical study, there is also an ongoing experimental research, performed in the MEKKA Laboratory at the Karlsruhe Institute of Technology (KIT). The experiments are carried out with the low-melting GaInSn alloy in a square duct with copper walls. Experimental measurements actually indicate a higher critical Reynolds number for time-dependent flow than expected from stability theory. The goal of our study is, therefore, twofold. First, we analyze the mechanisms of instability and associated phenomena, such as "banana" or Ting-Walker vortices (Kinet *et al.*, 2009) that appear in the region of sidewall jets. Secondly, we also aim to reproduce conditions close to that of the experimental test-loop at KIT in order to examine stability thresholds of the side-wall jets. These open questions are studied by the A3 project within the Helmholtz alliance LIMTECH (liquid metal technologies).

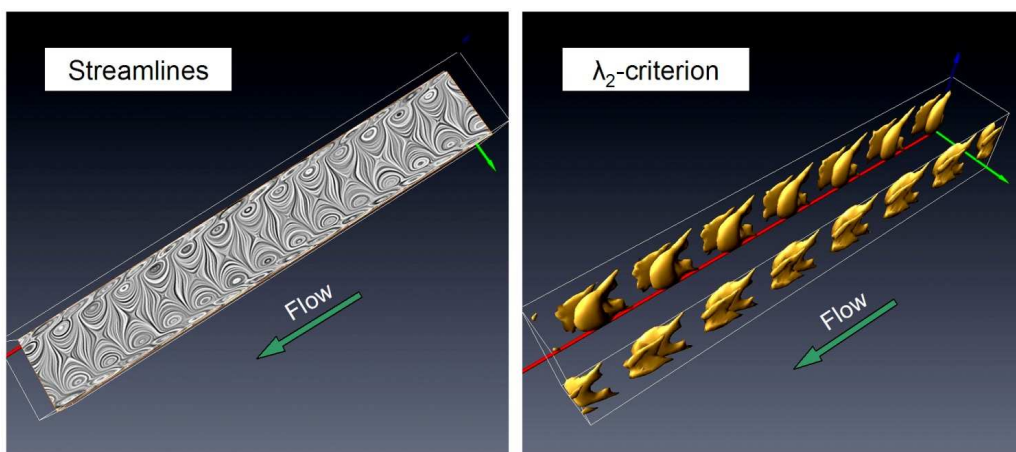


Figure 2: Appearance of the Ting-Walker ("banana") vortices in the region of sidewall jets for Hunt's flow and perfectly conducting Hartmann walls in a direct numerical simulation at  $Re = 500$ ,  $Ha = 100$ . Shown are the streamlines in the  $(x, y)$ -midplane (left) and the isosurfaces of  $\lambda_2$ -criterion (right), where  $\lambda_2$  is the second eigenvalue of the tensor  $S_{ik}S_{kj} + \Omega_{ik}\Omega_{kj}$ .

## 2 Mathematical model and numerical method

### 2.1 Governing equations for low- $Re_m$ MHD flows

We consider the flow of an incompressible, electrically conducting fluid subjected to a uniform magnetic field  $\mathbf{B}_0$ . The flow is driven by a pressure gradient  $\partial P_0/\partial x$  in the streamwise  $x$ -direction. In the limit of low magnetic Reynolds number  $Re_m$ , the so-called quasi-static approximation Roberts (1967) can be applied. The fluctuating part  $\mathbf{b}$  of the magnetic field due to fluid motion is much smaller than the external magnetic field:  $\mathbf{b} \ll \mathbf{B}_0$ . The Lorentz force, therefore, reduces to

$$\mathbf{F} = \mathbf{j} \times \mathbf{B}_0, \quad (1)$$

where the induced electric current density is given by Ohm's law

$$\mathbf{j} = \sigma (-\nabla\phi + \mathbf{v} \times \mathbf{B}_0). \quad (2)$$

Here  $\mathbf{v}$  is the velocity vector,  $\sigma$  the electrical conductivity and  $\phi$  the induced electric potential.

If displacement currents are neglected and the fluid is assumed electrically neutral, the current density  $\mathbf{j}$  should satisfy the divergence-free constraint  $\nabla \cdot \mathbf{j} = 0$ . Thus, the electric potential  $\phi$  can be expressed via the following equation:

$$\nabla^2\phi = \nabla \cdot (\mathbf{v} \times \mathbf{B}_0). \quad (3)$$

In that case, the governing non-dimensional Navier-Stokes equations, including the Lorentz force term, become:

$$\frac{\partial \mathbf{v}}{\partial t} + (\mathbf{v} \cdot \nabla)\mathbf{v} = -\nabla p + \frac{1}{Re}\Delta\mathbf{v} + N(\mathbf{j} \times \mathbf{e}), \quad (4)$$

$$\nabla \cdot \mathbf{v} = 0, \quad (5)$$

$$\mathbf{j} = -\nabla\phi + \mathbf{v} \times \mathbf{e}, \quad (6)$$

$$\Delta\phi = \nabla \cdot (\mathbf{v} \times \mathbf{e}). \quad (7)$$

These non-dimensional equations are based on a characteristic velocity  $U$  and characteristic length  $L$ . In the case of flow in a square duct, they correspond to the mean velocity and the half-height of the duct. The units of time, electric potential and current density are  $L/U$ ,  $UB$  and  $\sigma UB$ , where  $B$  is the magnitude of  $\mathbf{B}_0$ . The unit vector  $\mathbf{e}$  is parallel to  $\mathbf{B}_0$ .

The dimensionless parameters are the Reynolds number

$$Re = UL/\nu \quad (8)$$

and the interaction parameter

$$N = \frac{Ha^2}{Re} = \frac{\sigma B^2 L}{\rho U}, \quad (9)$$

where  $\rho$  denotes the density and  $\nu$  the kinematic viscosity of the liquid metal.

The boundary conditions for velocity at duct walls are zero slip conditions  $\mathbf{v} = 0$ . The solution of Poisson equation (7) for the electric potential also requires boundary conditions. These are either Neumann type  $\frac{\partial \phi}{\partial n} = 0$  for perfectly insulating walls or Dirichlet type  $\phi = const.$  for the case of perfectly conducting walls. The case of finite wall conductivity requires a non-trivial treatment of the boundary conditions for the electric potential  $\phi$ . This special case is described further in the next sections.

## 2.2 Finite-difference solver

We have developed a DNS code for MHD flows in rectangular channel and duct geometries. It is based on the finite-difference method with collocated grid arrangement. The boundary conditions are periodic in the streamwise  $x$ -direction and no-slip for the wall-normal  $y, z$ -directions. In case of channel flow, the boundary conditions can be set to periodic in the spanwise  $y$ -direction. Below we present the general structure of the solver and component of the finite difference scheme.

We solve the system of governing equations (4–7). The time discretization is based on the fully explicit Adams-Bashforth/Backward-Differentiation method of second order (Peyret, 2002). The incompressibility condition is satisfied by applying the standard projection method. The entire procedure of advancing from the time layer  $n$  to  $n + 1$  can be presented as follows:

$$\text{Solve electric potential equation } \nabla \cdot (\nabla \phi^n) = \nabla^2 \phi^n = \nabla \cdot (\mathbf{v}^n \times \mathbf{e}) \quad (10)$$

$$\text{Compute electric current } \mathbf{j}^n = -\nabla \phi^n + (\mathbf{v}^n \times \mathbf{e}) \quad (11)$$

$$\text{Compute } \mathbf{F}^n = -(\mathbf{v}^n \cdot \nabla) \mathbf{v}^n + \frac{1}{Re} \nabla^2 \mathbf{v}^n + N (\mathbf{j}^n \times \mathbf{e}) \quad (12)$$

$$\text{Compute intermediate velocity field } \frac{3\mathbf{v}^* - 4\mathbf{v}^n + \mathbf{v}^{n-1}}{2\Delta t} = 2\mathbf{F}^n - \mathbf{F}^{n-1} \quad (13)$$

$$\text{Solve pressure equation } \nabla \cdot (\nabla p^{n+1}) = \nabla^2 p^{n+1} = \frac{3}{2\Delta t} \nabla \cdot \mathbf{v}^* \quad (14)$$

$$\text{Add pressure correction to restore solenoidal velocity field } \mathbf{v}^{n+1} = \mathbf{v}^* - \frac{2}{3} \Delta t \nabla p^{n+1}. \quad (15)$$

The boundary conditions for pressure at solid walls are obtained by direct projection of (15) on the normal to the wall:

$$\frac{\partial p^{n+1}}{\partial n} = \frac{3}{2\Delta t} \mathbf{v}_n^*. \quad (16)$$

The computational grid is orthogonal and can be clustered in the wall-normal directions  $y$  and  $z$  to resolve thin MHD boundary layers, which becomes particularly important for MHD flows

at high  $Ha$ . A non-uniform grid is generated by applying coordinate transformation. Currently two types of grid stretching can be applied, it is either a hyperbolic tangent or a modified Gauss–Lobatto distribution

$$z = d \frac{\tanh(A\zeta)}{\tanh(A)} \quad z = d(A \sin(\zeta\pi/2) + (1 - A)\zeta). \quad (17)$$

Here  $d$  is the channel half-width,  $-1 < \zeta < 1$  is the uniformly distributed coordinate,  $z$  is the wall-normal coordinate and  $A$  is the parameter that accounts for the strength of clustering. We also note that it is possible to implement virtually any grid transformation.

For spatial discretization we use a highly conservative scheme, proposed in Morinishi *et al.* (1998) for incompressible flows and extended in Ni *et al.* (2007a) and Ni *et al.* (2007b) to the case of low- $Re_m$  MHD. The scheme is of the second order of approximation. The discretization is conducted directly on the non-uniform grid with collocated arrangement. The solution variables  $\mathbf{v}$ ,  $p$ ,  $\mathbf{j}$ , and  $\phi$  are stored at the same grid points, the equations (10–15) are approximated at these points too. The Poisson problems for pressure and electric potential are solved in the Fourier space by applying the fast Fourier transform (FFT) in the streamwise direction  $x$ . After that the elliptic problem

$$-k^2 \hat{p}(y, z) + \Delta_{yz} \hat{p}(y, z) = \widehat{rhs}(y, z)$$

is solved for each streamwise wavenumber  $k$  with the  $2D$  cyclic reduction method, a part of the software library Fishpack (Adams *et al.*). Details are provided in Krasnov *et al.* (2011).

For the effective use of the modern massive-parallel computers the code is parallelized with domain decomposition using the MPI library and parallel threads using Open MP. This hybrid approach allows performing simulations at very large computational resolution (of the order of  $10^9$  points), which is a necessary prerequisite for wall-bounded MHD flows at high  $Ha$  and  $Re$  numbers, where small-scale turbulence and thin boundary layers are typically present.

During the work on the project A3 the code has undergone several additional modifications. One part of these modifications is the implementation of non-periodic in-/out-flow conditions (Zikanov *et al.*, 2013). The other extensions, aimed to improve performance and to tackle specific conditions in the case of duct flows with conducting walls, are described below.

### 2.3 Implicit scheme for viscous terms

The first modification concerns the diffusive terms  $\frac{1}{Re} \nabla^2 \mathbf{v}$ , which can now be treated either explicitly (as in eq. (12)) or implicitly. The implicit treatment has been implemented to tackle flow regimes at low  $Re$  numbers and/or high  $Ha$ . In both cases the viscous terms can become a source of numerical instability, either because of low  $Re$  or due to overly strong grid clustering at the walls, which also imposes severe limitations on the time step. The implicit

treatment of diffusive terms involves three additional elliptic problems to be solved for all three velocity components, therefore, computational time per integration time step increases. Our benchmarks with the implicit scheme show that its performance is about two to three times slower than the fully explicit version. At the same time, for Reynolds numbers  $Re < 2000$  or Hartmann numbers  $Ha > 200$  the time-step can be up to  $10^2$  times higher. As a result, for a certain combination of parameters that is typically associated with a requirement of strong grid clustering, the computational efficiency can benefit from the implicit scheme, since the overall speed-up may increase by factor of 10 to 20. More details on the performance issue are provided further in section 3.1.

## 2.4 Boundary conditions for finite-wall conductivity

Another important modification amounts to imposing a different type of boundary conditions for the solution of the Poisson problem for the electric potential  $\phi$ . In case of ideally conducting walls the problem is solved with Dirichlet boundary conditions  $\phi = 0$  at the walls, i.e. the wall-normal component  $j_n$  of the electric current may be non-zero and, hence, currents may flow into the wall.

The case of finite wall conductivity is treated following the so-called thin-wall approximation originally developed by Walker (1981). Within this approach the solution of the electric currents in the walls can be avoided, which means that the MHD equations have to be solved within the fluid domain only. The current flow in the wall is taken into account by imposing a special type of boundary condition for the electric potential  $\phi$ :

$$\partial\phi/\partial n = C_w\Delta_\tau\phi. \quad (18)$$

Here  $n$  and  $\tau$  are, correspondingly, the wall-normal and wall-parallel directions, and  $\Delta_\tau$  is the Laplacian in the plane of the wall. The parameter  $C_w$  is the wall conductance ratio, which depends on the wall thickness and the ratio between conductivities of fluid and walls.

The elliptic solver Fishpack (Adams *et al.*) can only tackle relatively simple forms of boundary conditions, such as non-homogeneous Neumann- and Dirichlet-types or a mixed condition  $\partial\phi/\partial n + \alpha\phi = r$ , where  $\alpha$  is a constant. Therefore, in order to satisfy the non-trivial condition (18), the numerical procedure of finding the electric potential involves additional iterations. As a result, each integration time-step  $\delta t$  requires more computation. We have implemented several iterative schemes aimed to improve convergence and minimize the overall computational overhead.

The first method is rather straightforward and similar to that of Sterl (1990). The only significant difference is that in the study (Sterl, 1990) the problem is solved with Dirichlet boundary conditions, i.e. starting the iterations from the case of ideally conducting walls, whereas we do it other way around. We solve the Poisson problem with the Neumann conditions

and update the normal derivative every iteration from  $\partial\phi^m/\partial n = C_w\Delta_\tau\phi^*$ , where  $\phi^* = \omega\phi^m + (1 - \omega)\phi^{m-1}$  and  $m$  is the iteration counter. Under-relaxation is still needed. We have found that the value of the relaxation coefficient  $\omega = C_w/2$  suggested by Sterl (1990) also works in our modified procedure.

The convergence of the proposed iterative procedure can be further improved, which has been done in the next step. In general, convergence of iterative schemes greatly benefits from semi-implicit treatment, i.e. a part of the terms is represented implicitly. The modification is fairly obvious for the full 3D problem considered in the Fourier space. Assuming we solve the problem  $\partial\phi/\partial z$  at the  $z = \pm 1$  wall and  $\tau$  being the  $(x, y)$ -surface, we can split the 2D Laplace operator  $\Delta_\tau$  into two parts  $-k^2\hat{\phi} + \partial^2\hat{\phi}/\partial y^2$ , where  $k$  is the streamwise wavenumber and  $\hat{\phi}$  is the Fourier coefficient. In this case equation (18) can be rewritten in this form  $\partial\hat{\phi}/\partial z + C_w k^2\hat{\phi} = C_w\partial^2\hat{\phi}/\partial y^2$  and the modified version of the iterative scheme becomes  $\partial\hat{\phi}^m/\partial z + C_w k^2\hat{\phi} = C_w\partial^2\hat{\phi}^*/\partial y^2$ . The terms on the left hand side include the wall-normal derivative and the streamwise part of the Laplace operator  $\Delta_\tau$  that can be jointly used to form a mixed boundary condition for the Fishpack solver. We have performed benchmarks with this implementation. The tests show that, depending on the resolution and near-wall grid stretching, convergence is achieved in about 5–7 iterations.

Finally, we also note that this principle can be extended further to the remaining term  $\partial^2\hat{\phi}/\partial y^2$  on the right-hand side. This derivative is actually approximated by a finite-difference stencil of 2<sup>nd</sup> order, which in case of a non-uniform  $y$ -grid and function  $f$  is

$$\delta_{yy}f_j = \frac{(f_{j+1} - f_j)(y_j - y_{j-1}) - (f_j - f_{j-1})(y_{j+1} - y_j)}{(1/2)(y_{j+1} - y_{j-1})(y_{j+1} - y_j)(y_j - y_{j-1})}.$$

One can absorb all the terms and coefficients at point  $j$  and move them to the left-hand side so the mixed boundary condition will resemble almost the same form  $\partial\hat{\phi}/\partial z + \alpha(y)\hat{\phi} = \hat{r}(y)$ . Here  $\alpha(y)$  contains the streamwise coefficient  $k^2$  and the  $j$ -coefficients from the finite-difference approximation, whereas the remaining terms, denoted as  $\hat{r}$ , represent the explicit right-hand side. In this formulation the coefficient  $\alpha$  varies along  $y$ -coordinate and Fishpack cannot tackle mixed boundary conditions when  $\alpha$  is not a constant. We have, therefore, implemented one more method, replacing Fishpack by another solver from the Mudpack library (Adams). The solver is based on the hybrid approach, including both multigrid and direct methods for elliptic problems, and allows one to specify mixed boundary conditions in “non-separable” form, i.e. with  $\alpha$  varying along  $y$ . The drawback of this approach is that there are two iterative loops involved: the usual iterations over the  $\phi$ -field and multigrid cycles. The latter obviously makes conclusions about improvements in convergence less straightforward. This particular approach will be the subject of further work on improving the numerical method.



### 3 Results of simulations

In this section we describe results of our direct numerical simulations, performed in a broad range of  $Re$  and  $Ha$  numbers ( $Re \leq 50000$  and  $Ha \leq 1000$ ). The simulations aimed at identifying unstable regimes have been carried out with idealized conditions, i.e. with perfectly conducting Hartmann walls. The more realistic boundary conditions implemented in our code (section 2.4) have not been used so far in fully  $3D$  simulations. The reason is that this approach comes with a significant overhead for the computation of the electric potential. We plan to extend our research and address the effects of finite wall conductivity as the next step after completion of the present study.

#### 3.1 Benchmarks for laminar duct flow

Before proceeding with production simulations we have performed a series of verifications and benchmarks of our in-house DNS solver for laminar flows in square duct with conducting Hartmann walls. The solver had been successfully tested and applied in several studies for simulations of MHD flows in ducts with insulating walls. However, the case of Hunt's flow, in particular regimes at high  $Ha$ , obviously pose additional difficulties to be checked for full confidence.

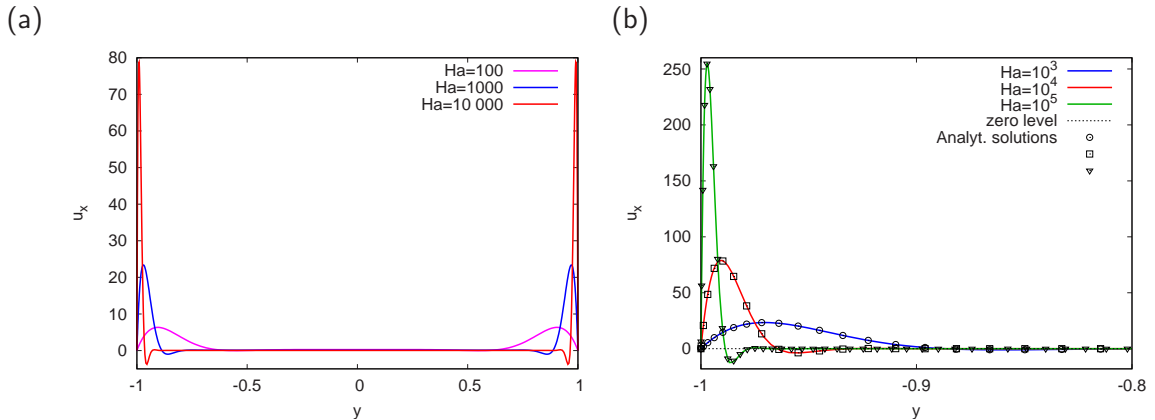


Figure 3: Results of numerical simulations for laminar Hunt's flow. (a) Basic velocity profile along the  $y$ -direction showing sidewall jets for  $Ha = 100, 10^3$  and  $10^4$ ; (b) zoom into the near-wall region and comparison with analytical results for  $Ha = 10^3, 10^4$  and  $10^5$ . The resolution in  $(y, z)$ -plane is  $256 \times 256$  points, grid clustering is set by hyperbolic tangent (17) with stretching coefficients  $A_y = 3.5$  and  $A_z = 4.0$  in the  $y$ - and  $z$ -directions, correspondingly.

The first step was to check the numerical results versus analytical solutions. This verification has been done within a wide range of  $Ha$  numbers varying from 100 to  $10^5$ . The Reynolds number  $Re$  was kept constant at 1000 since the laminar solutions do not depend on  $Re$ . Figure 3(a) demonstrates the general effect of magnetic field on the side-wall jets for  $100 \leq Ha \leq 10^4$  and gives an overview of the associated numerical difficulties. One can see that the side-wall jets become gradually thinner and the maximum velocity increases with  $Ha$ . The laminar side-

wall jets, i.e. their thickness and the maximum velocity, scale as  $Ha^{1/2}$ , thus the problem at high  $Ha$  becomes non-trivial for numerical treatment. We have also performed an additional verification and found that in rescaled units for both velocity and wall distance (proportional to  $Ha^{1/2}$ ) the profiles collapse into essentially one single curve. Verification versus analytical solution (series expansion) is illustrated in Figure 3(b). Here the range of  $Ha$  is extended to the value of  $10^5$  and only the near-wall behavior is shown ( $-1 < y < -0.8$ ). The detailed comparison indicates that the solver is in complete agreement with the analytical solution even at extreme values of  $Ha$ .

We note that these tests were also used as an opportunity to benchmark versions of the code with explicit or implicit treatments of the viscous terms  $\frac{1}{Re}\nabla^2\mathbf{v}$ . The verification simulations – essentially  $2D$ , since laminar solutions are uniform along the streamwise coordinate  $x$  – have been conducted at the numerical resolution of  $256 \times 256$  points per  $(y, z)$ -plane and the same grid stretching set by a hyperbolic tangent (17) with stretching factors  $A_y = 3.5$  and  $A_z = 4$ . We have found that for  $Ha \sim 10^3$  the implicit treatment of viscous terms is beneficial for overall performance. For example, simulations performed at  $Ha = 1000$  show that the integration time-step  $\delta t$  can be safely increased by at least a factor of 100 without loss of numerical stability. This situation, however, changes with the growth of  $Ha$  and, for  $Ha \approx 10^4$ , the explicit version becomes faster. The reason is that at high  $Ha$  (more precisely at large interaction parameter  $N = Ha^2/Re$ ) the stability properties of the scheme and, correspondingly, the integration time-step are governed by the MHD term (see Kinet (2009)). The MHD terms are fully explicit, thus, the specific treatment of viscous terms becomes irrelevant for regimes at large  $N$ .

As the second step, we have verified the implementation of boundary conditions for electric potential corresponding to the case of finite wall conductivity. Verification has been done by reproducing test cases from the original study (Sterl, 1990), namely two values of the Hartmann number,  $Ha = 100$  and  $1000$ , and the wall conductance ratio  $C_w = 0.1$ . The simulations have been performed with the implicit solver at  $96 \times 96$  grid points in  $y$ - and  $z$ -directions, grid clustering is set by hyperbolic tangent (17) with  $A_y = A_z = 3$ . The results for laminar flow in a square duct are shown in Fig. 4. The basic velocity profiles for the cases of ideally conducting Hartmann walls are shown for comparison to highlight the effect of finite conductivity. Our numerical results show that the obtained maximum velocities (peak values) as well as the mid-cut distributions are in perfect quantitative agreement with Sterl (1990).

### 3.2 Results at low- $Ha$ regimes, jet detachment

As pointed out in the introduction, the sidewall jets are highly unstable even for relatively low  $Re$ . Thus, the parameters of simulations in this part of the study were kept at  $Re < 10000$  and  $Ha < 500$  to capture the beginning of flow instability. There is an obvious ambiguity in exploring the parameter space – one can vary one of the parameters ( $Re$  or  $Ha$ ), while

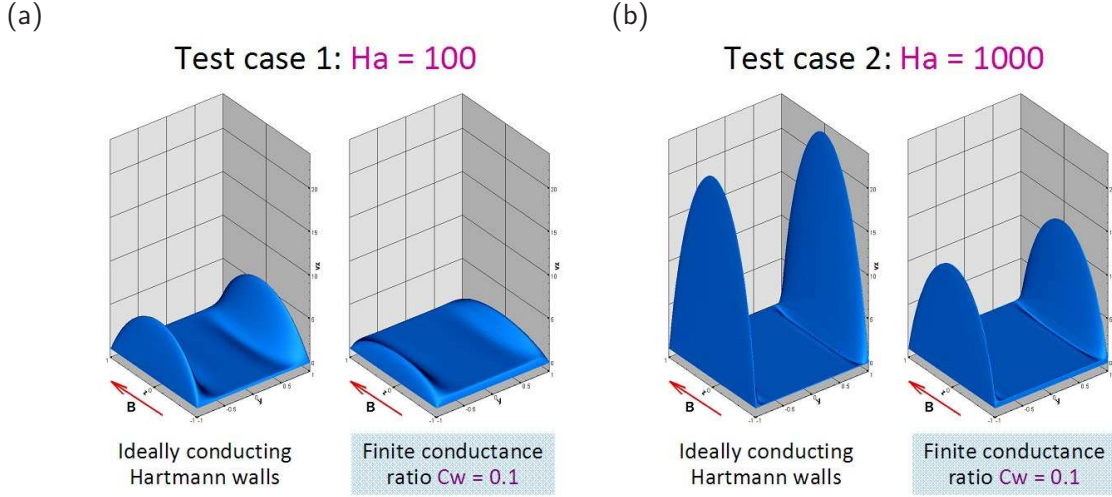


Figure 4: Results of DNS for laminar Hunt's flow at  $Ha = 100$  (left),  $Ha = 1000$  (right). For each  $Ha$  number two cases are shown: ideally conducting Hartmann walls and the case of finite wall conductivity with wall conductance ratio  $C_w = 0.1$ .

the other remains fixed. Since the laminar basic profile is governed by the  $Ha$  number only, the sources of instability – inflection points located on the basic profile – do not explicitly depend on  $Re$ . Therefore, we have performed simulations at fixed  $Ha$  and have varied  $Re$ . This approach was also employed in a prior study (Kinet *et al.*, 2009).

Unsteady solutions of wall-bounded shear flows can be obtained in different ways. Here we mention two of them. The first approach uses fully developed non-MHD turbulent flow, precomputed for the closest possible value of  $Re$ , as the initial state. The magnetic field is then switched on and the simulation is continued further (section 3.3). In another scenario the unsteady MHD solution, obtained for a certain  $Re$ , is used to study evolution towards a different target  $Re$ , which can be either higher or lower than the initial value. The second approach has been most extensively used in this section on low- $Ha$  and also to study the phenomenon of multiple states or hysteresis (section 3.4). Both ways of changing  $Re$  have been employed – with small steps (either increments or decrements) and as a single shot to the target value.

The onset of instability (settling of unsteady or time-dependent regimes) was detected by monitoring the kinetic energy of the transverse velocity components  $q_t = u_y^2 + u_z^2$ . This quantity has been confirmed as a very reliable indicator as suggested by our prior studies (Krasnov *et al.*, 2013; Zikanov *et al.*, 2013). The simulations have been conducted for two streamwise domain lengths  $L_x = 4\pi$  and  $8\pi$ , and numerical resolution varying from  $512 \times 96^2$  to  $1024 \times 128^2$  points. As it will be shown further, the longer domain becomes essential when the TW side-wall vortices are transformed into streamwise elongated structures upon increasing  $Re$ . To attain a statistically sustained (fully developed) state the simulations have typically run for the time from at least 100 to 1000 convective time-units.

We begin with the results of simulations at  $Re = 500$  and  $Ha = 100$  where the first appearance of instability was already detected. The structures evolving in the side-layers are shown in Fig.

2. Visual inspection of the streamline plot suggests the same view as in the study of Ting *et al.* (1991). Vortices, located within the area of each side-wall, appear as pairs consisting of clockwise (CW) and counterclockwise (CCW) rotating structures. Hereafter the rotation is defined in respect to the right-side if viewed along the flow direction. These vortices are in a staggered arrangement and tend to elongate in the vertical direction. The vertical elongation is particularly well seen around the middle section  $z = 0$ , as indicated by the  $\lambda_2$ -plot in Fig. 2. According to Jeong & Hussein (1995), negative regions of  $\lambda_2$  identify coherent vortical structures ( $\lambda_2$  is the 2<sup>nd</sup> eigenvalue of the tensor  $S_{ik}S_{kj} + \Omega_{ik}\Omega_{kj}$ , where  $S_{ij}$  and  $\Omega_{ij}$  are the rate of strain and vorticity tensors, correspondingly). However, the size of the TW vortices seems somewhat bigger than initially believed (Ting *et al.*, 1991). Further increase of  $Re$  demonstrates that the TW vortices continue to grow in size and energy until, at about  $Re = 1000$ , transformation to another flow regime takes place. Here the unsteady flow is represented by large-scale vortical structures, which exhibit elongation in the streamwise direction and occupy about 60% of the fluid domain. Their kinetic energy is at least 3 times higher than that of the TW vortices and is largely – up to 80% – associated with the streamwise velocity component  $u_x$ .

Beginning at  $Re \approx 1600$  we have found another type of instability, a new regime that appears as partial detachment of the side-wall jets along the streamwise direction. Partial jet detachment from the side walls of a duct is not a completely new phenomenon as it was first observed by Kinet *et al.* (2009). They stated that partial detachment was the development of large and small scale eddies located within the side-wall jets, which influenced the near wall flow structure. The core still remained a flat laminar flow.

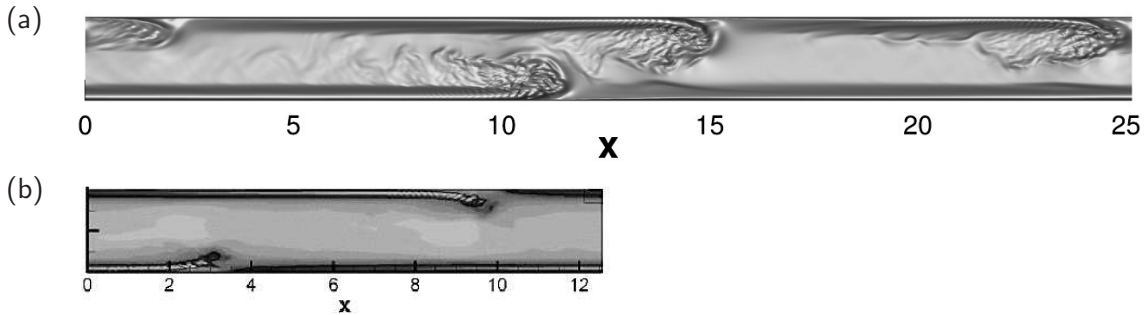


Figure 5: Results of numerical simulations of Hunt's flow at  $Ha = 100$ . Flow states with first appearance of jet detachments are shown for two domain sizes:  $L_x = 8\pi$  and  $Re = 1630$  (top) and  $L_x = 4\pi$  and  $Re = 1500$  (bottom). Instantaneous patterns in the  $(x, y)$ -mid-plane at  $z = 0$  are visualized by the full-scale streamwise velocity component. Flow direction is from left to right, magnetic field vector is perpendicular to the  $(x, y)$ -plane.

Kinet *et al.* (2009) studied regimes in a fully conducting square duct with  $C_w = 0.5$ , where all walls can be viewed as quite good conductors. In these conditions the development of jet detachment was observed at  $Re \approx 3700$  and  $Ha = 200$ . In our simulations we have discovered that partial side-wall jet detachment occurs at much lower  $Re$  and  $Ha$  numbers. In the conditions of idealized Hunt's flow, jet detachment has already been observed at  $Ha = 100$

and  $Re > 1600$ , as shown in Fig. 5(a), which is a new flow regime. Here, large dominating clockwise (CW) rotating vortices are attracted to the inner wall region, which is being promoted by high shear. The smaller counter clockwise (CCW) rotating vortices are moved into the outer jet region.

During this study we have found that the initially chosen domain size  $L_x = 4\pi$  is not sufficient for several reasons. First, it can not properly address the evolution of detached structures, as can be seen in Fig. 5(b). The domain is obviously too short and can fit only one detachment at a side wall, which may potentially hamper further development of these structures. Secondly, we have also observed that simulations performed in the shorter domain consistently yield somewhat premature appearance of unstable regimes as, e.g., the onset of jet detachments shown in Fig. 5(b) has been observed at  $Re = 1500$ .

Our investigations at higher  $Re$  and longer domain size have confirmed this conclusion. Namely, it has been found that, upon increasing the Reynolds number, the detachments develop into a clearly pronounced staggered pattern along the side-walls, as demonstrated in Fig. 6(a) for  $Re = 2000$  and domain size  $L_x = 8\pi$ . One can also see that the core flow loses its almost unperturbed state, observed at much weaker instabilities, such as TW vortices. This happens due to detachments spreading deeper into the bulk region, which becomes involved into unsteady behavior.

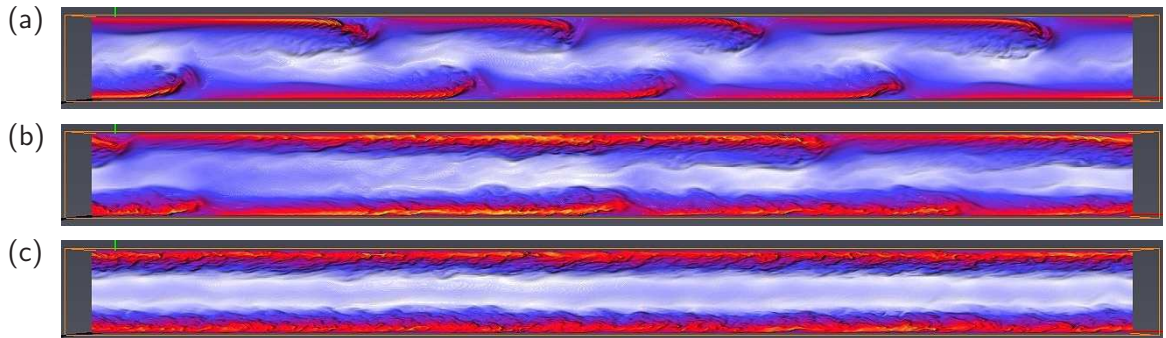


Figure 6: Transition of states with jet detachments towards fully turbulent side-wall jets at  $Ha = 100$  shown for  $Re = 2000$  (a), 4000 (b) and 5000 (c). Instantaneous patterns in the  $(x, y)$ -mid-plane are visualized by the full-scale streamwise velocity component. Flow direction is from left to right, magnetic field vector is perpendicular to the  $(x, y)$ -plane.

In addition to this newly observed flow regime, as  $Re$  is increased further, up to  $Re = 4000$  (Fig. 6(b)), the partially detached jets elongate in the flow direction and become increasingly turbulent, especially in the trailing “tail”. Basically, the detached jets almost lose their characteristic detachment profile, albeit a few residual detachments are still possible to spot. An interesting observation is that, upon increasing turbulization, the jets tend to stay closer to the side walls of the duct. Moving to  $Re = 5000$  (Fig. 6(c)) shows that the regime of jet detachments vanishes completely. At this point we first start to observe the development of a fully turbulent flow in the side-wall region. At the same time, as  $Re$  increases, the core flow becomes less involved into unsteady motion, compared to the regimes with jet detachments.

This behavior is observed almost up to  $Re = 10000$ , albeit the jets here become thicker and visibly begin to spread into the core region, as shown in Fig. 7. This suggests that regimes with fully turbulent duct flow, i.e. including the core, should be expected at even higher  $Re$ . Similar behavior in the development of instabilities has also been observed for simulations at  $Ha = 200$ . These runs are still ongoing and have to be fully completed to obtain a rounded picture for all considered Reynolds numbers up to 10000.

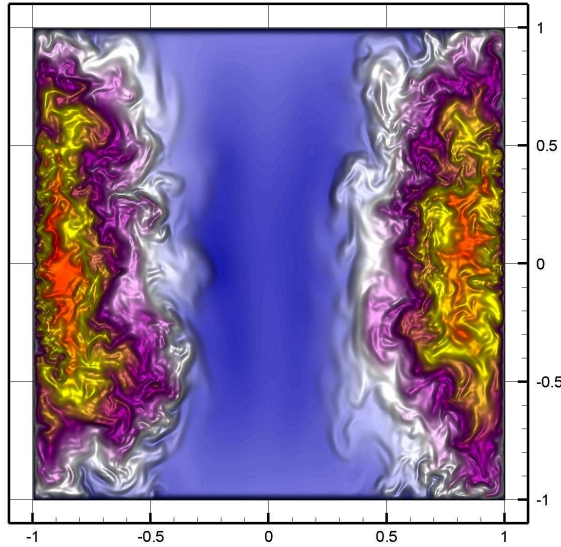


Figure 7: Instantaneous distribution of streamwise velocity at  $Re = 10000$  and  $Ha = 100$ , shown in the  $(y, z)$ -cross-section at  $x = L_x/2$ .

### 3.3 Results at high $Ha$ numbers

The goal of these simulations was to reach the range of parameters corresponding or similar to those in the actual experiments performed at KIT and to determine specific flow patterns and formations associated with unstable regimes. We have therefore performed a series of large-scale simulations for a square duct at  $Ha = 500$  and  $1000$  and Reynolds numbers  $Re$  from  $1000$  to  $50000$ . The numerical resolution was varied from  $1024 \times 256 \times 256$  to  $2048 \times 384 \times 384$  points with the domain size  $L_x = 8\pi$  in the streamwise direction. So far the case of ideally conducting Hartmann walls has been considered.

Here the procedure of obtaining unsteady flow regimes, discussed in section 3.2, was changed to avoid extremely long transient evolution. Our simulations at smaller  $Ha$  have shown that the transient evolution to the target  $Re$  may last hundreds or even thousands of convective time-units. Given the large resolution requirements for high  $Re$  and  $Ha$  numbers, the long computations for transient phases are not affordable. An obvious way to shorten this time would be to impose perturbation on the initially laminar flow. This approach has been widely employed in various studies on direct flow transition and has received different implementations.

The simplest way is to add random  $3D$  noise. A faster way to reach transition is by adding of specially constructed (optimal) perturbations. The disadvantage of this approach is that many parameters are involved, e.g. amplitude and shape of perturbations.

We have, therefore, adopted the method used in studies of inverse transition. Instead of laminar initial state, we have used fully developed non-MHD turbulent flows for each  $Re$  number. This approach requires additional simulations to be performed at the same grid size as MHD flows, which are used then as precomputed initial fields. After that the magnetic field is switched on and the simulation is continued further for the target parameter of  $Ha$ . This method helps to avoid ambiguities of externally imposed perturbations. It also has the appeal that fluctuations have been created in a natural way. One interesting observation for this approach is that the fluctuating energy of turbulent non-MHD flow drops by several orders of magnitude as the magnetic field is switched on, as shown in Fig. 8. Basically, the magnetic field rapidly destroys (almost kills off) turbulence so that remaining perturbations can be viewed as a residual noise. After a minimum is attained (at  $t \approx 110$  in Fig. 8) the residual fluctuations start to grow and finally evolve into another fluctuating/unsteady regime.

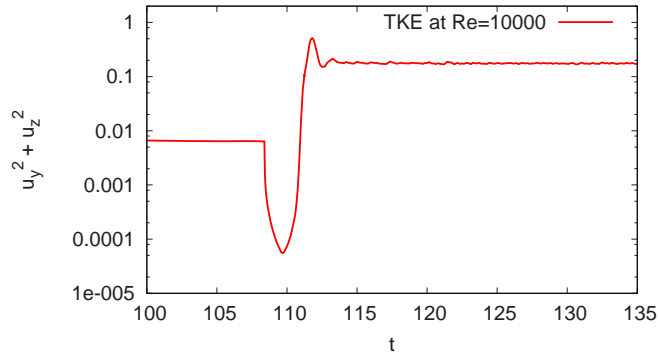


Figure 8: Evolution of kinetic energy of transverse velocity components. Transition from non-MHD turbulent flow to MHD flow at  $Ha = 1000$  and  $Re = 10000$  is shown.

We have also checked the robustness of obtained solutions using the procedure described in section 3.2. The obtained unsteady solutions have been used as initial states to study evolution of flow patterns at fixed  $Ha$  and changing  $Re$ . Here we note that no visible differences between both methods were found for  $5000 \leq Re \leq 50000$ . At lower  $Re$  the situation becomes somewhat different, cf. section 3.4.

We focus on the results at  $Ha = 1000$  as the highest value where the MHD effects should be most pronounced. Fig. 9 shows that at  $Re = 10000$  unsteady structures appear as patches of finite streamwise extent with pronounced alignment in the direction of the magnetic field. Visual inspection of the full-scale streamwise velocity at  $Re = 10000$  has clearly indicated that these structures are jet detachments, albeit tightly localized at the side-walls. Upon increasing the Reynolds number these patches are replaced by continuous bands occupying the full length of the duct. At the same time, the core region remains essentially unperturbed,

even at  $Re = 50000$ . This should be attributed to the effect of very strong magnetic field, e.g., the interaction parameter  $N = 20$  at  $Re = 50000$ , that keeps fluctuations confined in the side-wall regions and suppresses them in the bulk. The observation is different to the case of low- $Ha$  regimes ( $N = 1\dots 5$ ) described in the previous sections, where the core flow was strongly involved into unsteady motion at already  $Re \approx 1600$  (the first appearance of jet detachments) and later on at  $Re \approx 10000$  (turbulent jets start spreading in the bulk region). The results for perfectly conducting walls already show favorable agreement with the experiments of KIT where instability is detected by electric potential measurements.

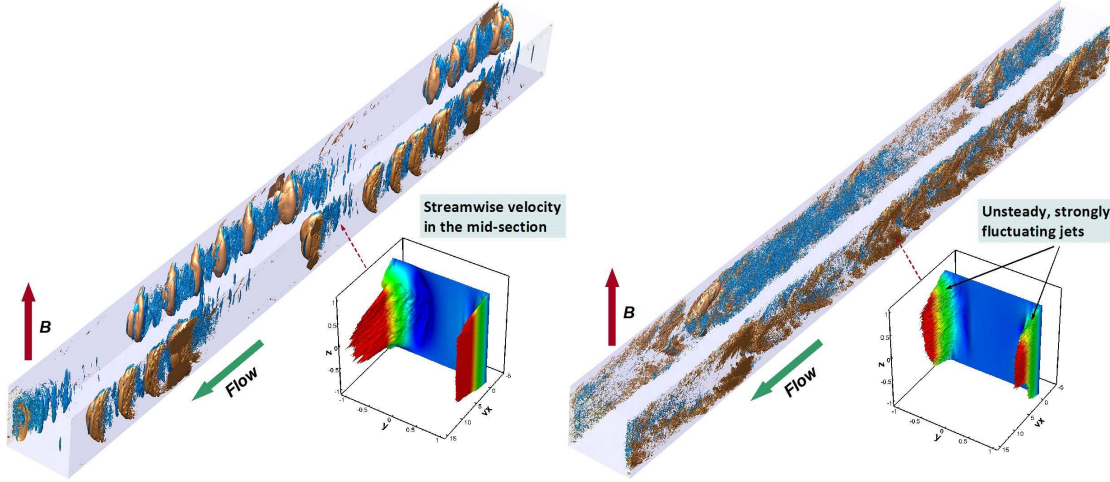


Figure 9: Unstable regimes of Hunt's flow at  $Ha = 1000$  and  $Re = 10000$  (left) and  $50000$  (right), results of DNS at  $2048 \times 384^2$  points with domain size  $8\pi \times 2 \times 2$ . The isosurfaces of turbulent kinetic energy (brown) of transverse velocity components  $u_y^2 + u_z^2$  are shown, also shown are the isosurfaces of the second eigenvalue  $\lambda_2$  (cyan) of the tensor  $S_{ik}S_{kj} + \Omega_{ik}\Omega_{kj}$ . The subplots also show unstable jet-like profiles of the streamwise velocity visualized in the cross-section at  $x = L_x/2$ .

### 3.4 Multiple states at low- $Re$ regimes

Another interesting aspect of Hunt's flow is the so-called multiplicity of solutions that we have obtained at low  $Re$  regimes. These regimes probably appear close to the critical states, i.e. thresholds between laminar and unsteady/turbulent solutions. The phenomenon is known from the prior studies of, for example, Hartmann duct and pipe flows, where various arrangements of patterned turbulence have been observed in the transitional parameter range (Krasnov *et al.*, 2013; Zikanov *et al.*, 2013).

Here we find similar behavior in the range of low  $Re$  numbers. In particular, our simulations at  $Ha = 1000$  and  $Re = 1000\dots 2000$  show that approaching the critical parameters either from above (high- $Re$  regimes) or from below (low- $Re$  state) may produce different solutions. A schematic drawing illustrates this in Fig. 10. Therefore, it appears very unlikely that instability thresholds of Hunt's flow at low- $Re$  can be identified in a clear-cut way. To address this issue of "multiplicity", for each combination of flow parameters we have performed several large-scale simulations with different initial states.

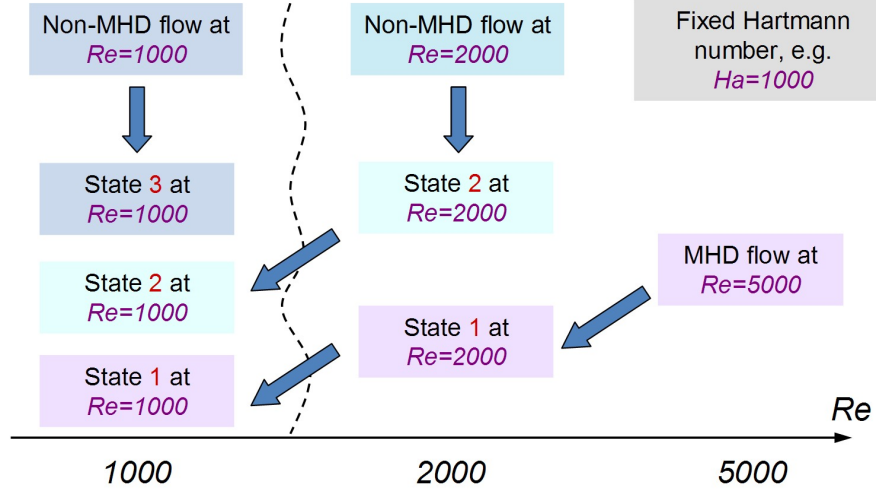


Figure 10: Illustration of the principle appearance of multiple states at low  $Re$  numbers, observed in the numerical simulations of Hunt’s flow. Three routes are shown: state 1 (pink) started from  $Re = 5000$  with strong jet detachments (see Table 1), “state 2” (cyan) and “state 3” (grey) initiated with fluctuating non-MHD flows at  $Re = 2000$  and  $Re = 1000$ , correspondingly. All 3 final solutions at  $Re = 1000$  correspond to states with jet detachments (see Table 1).

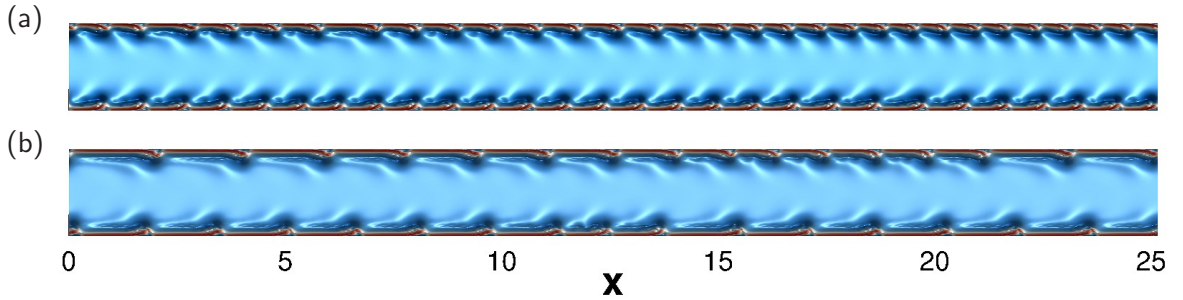


Figure 11: Results of DNS of Hunt’s flow at  $Re = 1000$  and  $Ha = 1000$  illustrating two different states, obtained while approaching the “target” parameters from different initial conditions: (a) route indicated as “state 1”, (b) route indicated as “state 2” in Fig. 10. Instantaneous patterns, showing instabilities at the side walls (jet detachments), are visualized by the full-scale streamwise velocity component in the  $(x, y)$ -mid-plane at  $z = 0$ . Flow direction is from left to right, the magnetic field vector is perpendicular to the  $(x, y)$ -plane. Results of DNS at  $1024 \times 256 \times 256$  points and domain size of  $8\pi \times 2 \times 2$  are shown.

An example of the obtained states with different flow patterns is shown in Fig. 11 for  $Re = 1000$ . Both identified solutions correspond to flow states with jet detachments, albeit the detached structures are rather weak, compared to similar regimes at higher  $Re$ . The obtained instabilities do not only differ by their arrangement at the side walls, but also the inner structure is not the same. The kinetic energy of transverse velocity fluctuations is different for both cases, too.

This difference is also reflected in the time- and streamwise-averaged mean velocities, as can be seen in Fig. 12, where the unsteady states and laminar solution are shown. In both cases of unsteady solutions the maximum velocity is about half of the value in the laminar case,

whereas the jets are much thicker. At the same time, we see that the jets obtained in “state 1” (corresp. to Fig. 11(a)) are slightly thicker and smaller in magnitude than those in “state 2” (corresp. to Fig. 11(b)). This can be attributed to the fact that the side-wall regions of “state 1” are populated with more detachments.

We note that similar behavior with multiple states (or hysteresis) has also been observed in the simulations at  $Ha = 100$ . Namely, we have found that in a series of decremental simulations (i.e. gradually decreasing  $Re$  from high- to low-values) the flow keeps to exhibit states with jet detachments until laminarization at  $Re = 200$ . Thus, all other instabilities, such as TW and large-scale vortices identified in the incremental simulations at  $500 < Re < 1500$ , have been completely passed by.

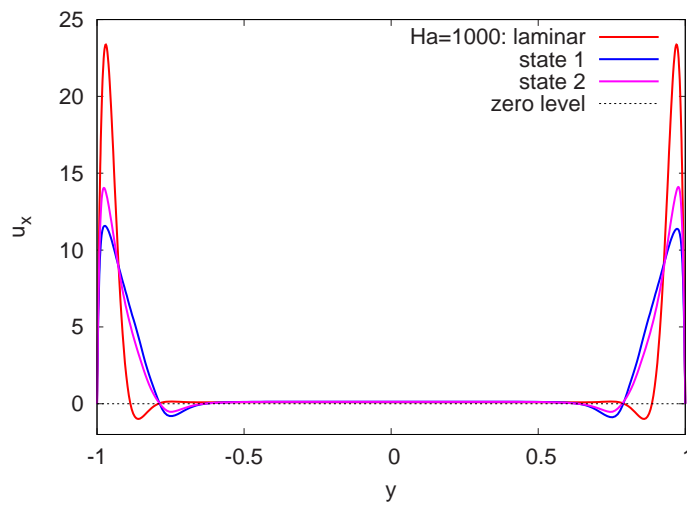


Figure 12: Time- and domain-averaged basic velocity profiles for Hunt's flow at  $Re = 1000$  and  $Ha = 1000$ . Two different flow regimes “state 1” and “state 2”, corresponding to those in fig. 11, are shown. Laminar velocity profile at  $Ha = 1000$  is shown for comparison.

$Ha$	$Re$	Resolution	State
100	500...1000	$1024 \times 128^2$	TW vortices
	1000...1500	$1024 \times 128^2$	Large-scale vortices
	1600...4000	$1024 \times 128^2$	Detach. jets
	5000	$1024 \times 128^2$	Turb. jets
	10000	$1024 \times 128^2$	TJ spread in the core
500	10000	$2048 \times 384^2$	Detach. jets
	20000	$2048 \times 384^2$	Turbulization of jets
	30000...50000	$2048 \times 384^2$	Fully turb. jets
1000	1000...2000	$1024 \times 256^2$	Detach. jets (weak), mult. states
	5000...20000	$2048 \times 384^2$	Detach. jets (strong, involving core)
	30000...40000	$2048 \times 384^2$	Localized turb. patches
	50000	$2048 \times 384^2$	Turb. bands at side-walls

Table 1: Parameters of MHD flow simulations and obtained states.

To check the robustness of the obtained solutions, the simulations have been conducted for about 100 convective time units. During this time no changes in the patterns have been observed. We can conclude that the obtained states are quite persistent branches within the variety of possible solutions or, probably, a much longer temporal evolution is required to capture further transitional behavior. We also note that these findings are, in fact, similar to the new unstable region (denoted as region “0”) observed in the recent KIT experiments at  $Re \approx 1000$  and  $Ha > 1300$ . The difference between experimental and numerical findings is likely due to the ideally conducting conditions in simulations, which could shift the range of  $Ha$  towards lower values.

The results of simulations discussed in sections 3.2 – 3.4 and the obtained unsteady solutions are summarized in Table 1.



## 4 Conclusions and outlook

The instability of Hunt's flow has been studied numerically within a wide range of  $Re$  and  $Ha$ , covering regimes of low and moderately high magnetic fields ( $Ha = 1000$ ). The latter approaches the range of parameters found in applications (cooling blankets for fusion reactors). Besides that, we have made an attempt to reproduce numerically conditions of the KIT experimental test loop.

Our simulations performed at  $Ha = 1000$  show that at low- $Re$  unstable regimes appear as partial jet detachments of rather short streamwise extent with pronounced alignment in the direction of the magnetic field. Upon increasing the Reynolds number these detachments are replaced by continuous bands occupying the full length of the duct. Our results for perfectly conducting walls already show favorable agreement with the experiments of KIT, where instability is detected by electric potential measurements.

We have also confirmed that the side-wall jets become thicker as the flow undergoes transition from laminar to unsteady solutions. In this transitional regime, the thickness of the jets is also shown to depend on the structures that evolve in the side-wall region. The specific arrangement and the total number of unsteady vortices may produce a pronounced effect on the side-wall jets and should influence integral parameters such as wall friction.

Our further steps will include detailed study of integral parameters, e.g. the analysis of total friction, pressure drop and potential difference, since these parameters are usually available in experimental studies. Finally, we plan to study instability phenomena in more realistic settings with finite wall conductivity taken into account. This will be aimed to approach as much as possible the actual conditions in the KIT experiments.



## References

- ADAMS, J. C. Mudpack: Multigrid software for elliptic partial differential equations. <http://www2.cisl.ucar.edu/resources/legacy/mudpack/>.
- ADAMS, J. C., SWARZTRAUBER, P. & SWEET, R. Efficient fortran subprograms for the solution of separable elliptic partial differential equations. <http://www2.cisl.ucar.edu/resources/legacy/fishpack>.
- BÜHLER, L. AND HORANYI, S. 2009 Measurements of time-dependent liquid metal magnetohydrodynamic flows in a flat rectangular duct. *Fusion Engineering and Design* **84**, 518–521.
- JEONG, J. & HUSSEIN, F. 1995 On the identification of a vortex. *J. Fluid Mech.* **285**, 69–94.
- KINET, M. 2009 MHD turbulence at low magnetic Reynolds number: Spectral properties and transition mechanism in a square duct. Doctoral thesis, Université Libre de Bruxelles, Bruxelles, Belgium.
- KINET, M., KNAEPEN, B. & MOLOKOV, S. 2009 Instabilities and Transition in Magnetohydrodynamic Flows in Ducts with Electrically Conducting Walls. *Phys. Rev. Lett.* **103**, 154501.
- KRASNOV, D., THESS, A., BOECK, T., ZHAO, Y. & ZIKANOV, O. 2013 Patterned turbulence in liquid metal flow: Computational reconstruction of the Hartmann experiment. *Phys. Rev. Lett.* **110**, 084501.
- KRASNOV, D., ZIKANOV, O. & BOECK, T. 2011 Comparative study of finite difference approaches to simulation of magnetohydrodynamic turbulence at low magnetic Reynolds number. *Comp. Fluids* **50**, 46–59.
- MORINISHI, Y., LUND, T. S., VASILYEV, O. V. & MOIN, P. 1998 Fully conservative higher order finite difference schemes for incompressible flow. *J. Comp. Phys.* **143**, 90–124.
- NI, M.-J., MUNIPALLI, R., HUANG, P., MORLEY, N. B. & ABDOU, M. A. 2007a A current density conservative scheme for incompressible MHD flows at a low magnetic Reynolds number. Part I: On a rectangular collocated grid system. *J. Comp. Phys.* **227**, 174–204.
- NI, M.-J., MUNIPALLI, R., HUANG, P., MORLEY, N. B. & ABDOU, M. A. 2007b A current density conservative scheme for incompressible MHD flows at a low magnetic Reynolds number. Part II: On an arbitrarily collocated mesh. *J. Comp. Phys.* **227**, 205–228.
- PEYRET, R. 2002 *Spectral Methods for Incompressible Viscous Flows*. New York: Springer.
- PRIEDE, J., ALEKSANDROVA, S. & MOLOKOV, S. 2010 Linear stability of Hunt's flow. *J. Fluid Mech.* **649**, 115–134.
- ROBERTS, P. H. 1967 *An introduction to Magnetohydrodynamics*. New York: Longmans, Green.

- STERL, A. 1990 Numerical simulation of liquid-metal MHD flows in rectangular ducts. *J. Fluid Mech.* **216**, 161–191.
- TING, A. L., WALKER, J. S., MOON, T. J., REED, C. B. & PICOLOGLOU, B. F. 1991 Linear stability analysis for high-velocity boundary layers in liquid-metal magnetohydrodynamic flows. *Int. J. Engng. Sci.* **29** (8), 939–948.
- WALKER, J. S. 1981 Magnetohydrodynamic flows in rectangular ducts with thin conducting walls. *Journal de Mécanique* **20**, 79–112.
- ZIKANOV, O., KRASNOV, D., LI, Y., BOECK, T. & THESS, A. 2013 Patterned turbulence in spatially evolving magnetohydrodynamic duct and pipe flows. *Theor. Comp. Fluid Dyn.* DOI: 10.1007/s00162-013-0317-y.





Pressure-driven magnetohydrodynamic duct flows in a transverse, wall-parallel and uniform field have been studied by direct numerical simulations with a conservative finite-difference method based on the quasi-static approximation of the induction equation and the thin-wall approximation to describe the finite wall conductance. The conducting Hartmann walls perpendicular to the magnetic field give rise to a laminar velocity distribution with strong jets at the side walls, which are susceptible to flow instability. Because of the substantial increase in computational cost associated with the finite wall conductance, high-resolution simulations have mainly been performed with perfectly conducting Hartmann walls and insulating side walls. The onset of time-dependent flow as well as fully-developed turbulent flow have been explored in a wide range of Hartmann numbers and Reynolds numbers. For the relatively low Hartmann numbers, time-dependence appears in the form of elongated so-called Ting-Walker vortices at the side walls of the duct, which tend to form staggered patterns along the streamwise direction. Upon increasing the Reynolds number these vortices are replaced by more complex eddy structures, and the jets partially detach from the walls. Eventually, the flow becomes turbulent also in the core. For high Hartmann numbers the flow displays localized patterns of Ting-Walker vortices near the side walls. The latter are replaced for higher Reynolds numbers by continuous turbulent bands that occupy the full length of the duct while the core of the flow still remains laminar.

ISSN 1869-9669  
ISBN 978-3-7315-0562-4

ISBN 978-3-7315-0562-4



9 783731 505624 >